Ogohara and Ro *Earth, Planets and Space* (2023) 75:10
https://doi.org/10.1186/s40623-023-01767-x

Earth, Planets and Space

EXPRESS LETTER

Open Access

Cloud trains associated with Martian Mountain Lee Waves on the eastern side of the Phlegra Montes

Kazunori Ogohara* and Maaya Ro

Abstract

Mountain lee waves have often been observed on the eastern side of the Phlegra Montes as wave trains visualized by water ice clouds in the Martian atmosphere. The seasonality and formation condition of these lee waves and associated cloud trains have not yet been investigated, whereas those of Martian dust storms have been studied observationally and numerically. We extract the cloud trains in this region from images observed by the Mars Orbiter Camera onboard the Mars Global Surveyor and measure the wavelengths of the lee waves. It is revealed that, on the eastern side of the Phlegra Montes, cloud trains tend to form in the northern winter season, except during the 2001 global dust storm. The results suggest that stationary mountain waves are excited in the thermally stable atmosphere, but are trapped below an altitude of approximately 10 km due to the zonal wind structure that increases rapidly with altitude. This is consistent with the previous studies on gravity waves in the Martian atmosphere and is the first study to constrain the typical altitude of the cloud trains from imager observations.

Keywords Mars, Mars atmosphere, Water ice cloud, Gravity wave

Graphical Abstract

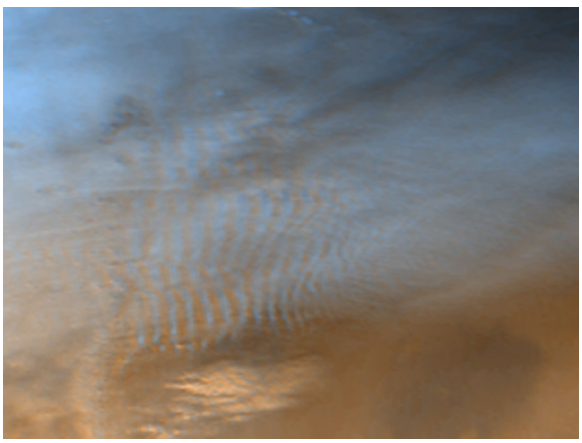

*Correspondence:
Kazunori Ogohara
ogohara@cc.kyoto-su.ac.jp
Full list of author information is available at the end of the article

Main text

Introduction

The present Mars environment is dry and cold. However, this does not mean that water ice clouds rarely form in the Mars atmosphere just because Mars is dry. Because of the low temperature of the atmosphere, the saturation vapor pressure of water remains low, so water vapor condenses relatively easily. Global distributions and seasonal variations in water ice clouds were revealed based on observations by the Mars Orbiter Camera (MOC) onboard Mars Global Surveyor (MGS) (Wang and Ingersoll 2002). The aphelion cloud belt (ACB) was precisely studied by several authors (e.g., Cooper et al. 2020, 2019; Guha et al. 2021). The roles of the ACB and the polar hood cloud on the global transport of water were investigated numerically (Montmessin et al. 2004). The advection of the water ice cloud contributes to the long-distance transport of water in the Mars atmosphere. The equatorward advection of the polar hood cloud by atmospheric waves prevents water from returning to the north polar cap and has a role of keeping the low latitude atmosphere wet. The clouds associated with some isolated peaks are also well reproduced by numerical simulations (Michaels et al. 2006; Wilson et al. 2007). Another type of cloud frequently observed in the Mars atmosphere is a cloud train associated with a mountain lee wave. Figure 1 shows a cloud train formed by a typical mountain lee wave observed on the east of the Phlegra Montes, which is visualized by several cloud streaks, and its counterpart on Earth. Such cloud trains are easily found in Mars images (e.g., Mars Daily Global Weather Maps, Wang and Ingersoll 2016) and become observations that provide the basis for implementing the gravity wave drag in numerical models (Forget et al. 1999). However, unlike dust storms, the cloud trains' seasonal variations and relations with the vertical distributions of wind and atmospheric stability have not yet been investigated, even focusing on a specific region.

In the present study, we extract cloud trains associated with mountain lee waves from visible images of Mars and reveal their seasonal variability around the Phlegra Montes. We also try constraining the altitudes of the lee wave propagation and the cloud train formation from the vertical profiles of zonal wind and temperature included in the Mars reanalysis dataset. The eastern side of the Phlegra Montes is close to one of the regions that is most prone to dust storms (Ogohara and Satomura 2011; Guzewich et al. 2015, 2017; Kulowski et al. 2017). Our results may lead to studies on relations between dust storm initiations and the atmospheric conditions deduced from mountain lee waves. The data used in the present study are described in the next section. The seasonal variations in the cloud train frequency and the wavelength are investigated in "Results and discussions" section. The background mean wind and atmospheric stability distributions where the lee waves are embedded are also discussed in "Results and discussions" section.

Materials and methods

Data

We used reflectance data from blue band (400–450 nm) images acquired by MGS/MOC (Malin et al. 2010), limiting our investigation of lee waves to the region centered around 180°E–40°N (west of the Arcadia Planitia, WAP). The selected region is shown in Fig. 2 with Mars topography. The Phlegra Montes is located near the western edge of the region. We examined 800 × 600-pixel (40° × 30°) subsets of the full-size MOC wide-angle camera (MOC-WA) image swathes. A total of 2,476 subsets were extracted from the MOC-WA images taken during

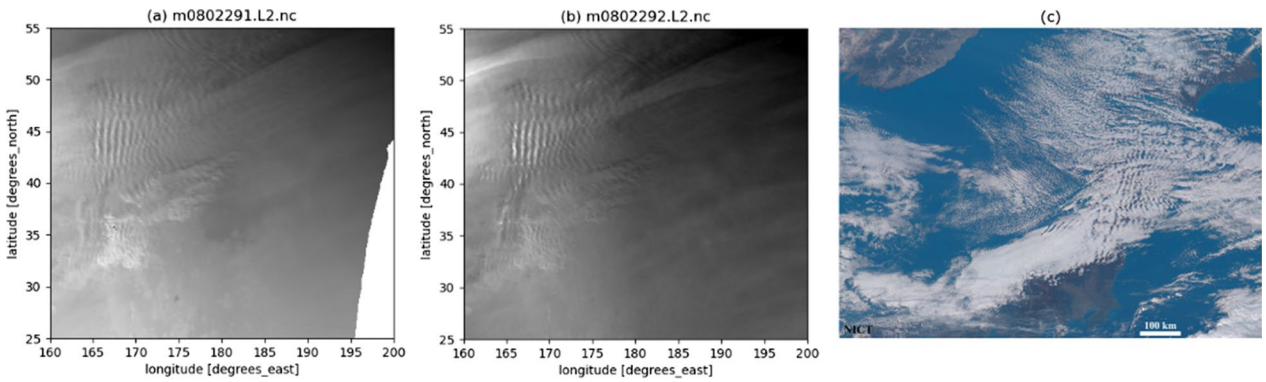

Fig. 1 An example of cloud trains on Mars and Earth. **a** and **b** are red and blue band images, respectively, observed in the eastern side of the Phlegra Montes by MGS/MOC on Oct. 10, 1999 (Mars Year 24 and solar longitude, $L_s = 222.17°$). A cloud train in the upper left part of each panel visualizes a lee wave. **c** is another example of terrestrial mountain lee waves observed by Himawari 8 on Nov. 17, 2016. The white bar in **c** corresponds to 100 km

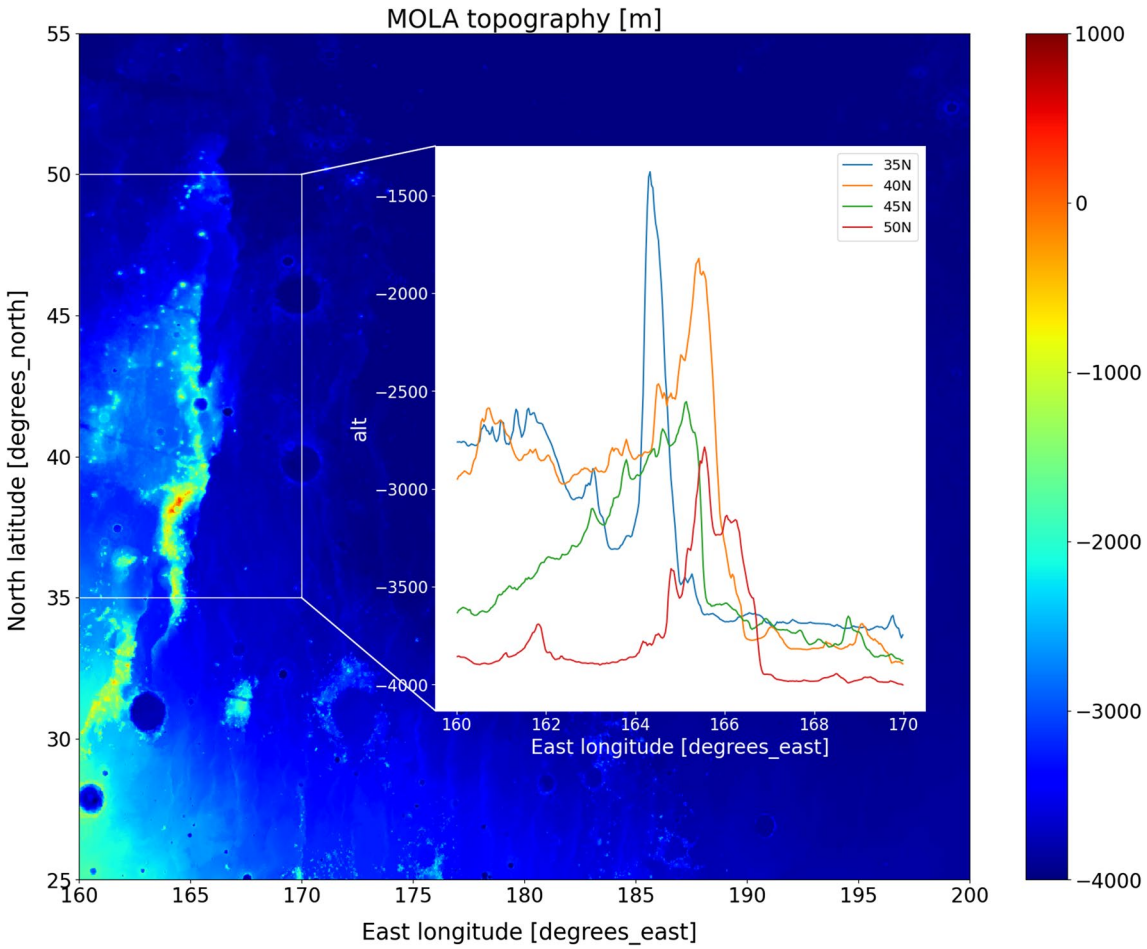

Fig. 2 Topography of the regions focused in this study. This was extracted from the topography data included in Mars Climate Database 5.0. Longitudinal distributions of the surface altitude of the Phlegra Montes at 30°N (blue), 40°N (orange), 45°N (green), and 50°N (red) are shown in the right part of the figure. 1 degree in longitude approximately corresponds to 45 km at 40°N

its mission period. Blue band images of MOC-WA were obtained through the Planetary Data System (PDS) Imaging Node. Noise reduction, radiometric calibration, and coordinate transformation to longitude–latitude coordinates were performed using Integrated Software for Imagers and Spectrometers (ISIS) (Sucharski et al. 2020). Opposition surge and low-frequency patterns of reflectance were removed from the images using the methods presented by Wang and Ingersoll (2002) and Ogohara et al. (2016). Areas with an incidence angle larger than 80° are filled with a missing value.

There is no wind observation data that can be used for investigation of the atmospheric condition when the cloud trains are formed. But the Mars reanalysis datasets, which are created from the combination of a numerical model and observations of other quantities (e.g., atmospheric temperature), are now available. The background mean dataset of the Ensemble Mars Atmosphere Reanalysis System (EMARS) version 1.0 (Greybush et al. 2019) was used to compare the frequency of the cloud trains with the seasonal variations in the thermal and wind structures around the region. It covers the MGS/MOC operation period and is consistent with the Thermal Emission Spectrometer (MGS/TES) retrievals that resolve the lower atmosphere (Conrath et al. 2000). The data are one-hour forecasts from the analysis mean dataset that were calculated in the sigma-p hybrid coordinate. In the present study, they are interpolated into the pressure coordinate in case of clarifying the relationship between the model vertical levels and the approximate altitudes ("Results and discussions" section).

Cloud train detection and wavelength measurement

Since upward wind associated with a lee wave is visualized by cloud streaks, cloud trains were detected by visually inspecting all extracted subsets. Cloud trains were not confused with other types of water ice clouds (e.g., clouds spreading over the northern high latitudes,

front-like clouds associated with baroclinic waves) because of their unique multi-streak textures. We can also visually determine the western and eastern edges of the cloud train. The two edge points of each cloud train were determined so that the line passing through them was as perpendicular as possible to the phase lines of the lee wave visualized by cloud streaks on the conformal projection image. The two red circles in Fig. 3 are the two edge points of the cloud train. The red line in Fig. 3 is locally perpendicular to the phase lines. The yellow circles in Fig. 3 indicate the two edge streaks on the red line, the most outside cloud streaks that can be visually detected. The mean wavelength of the lee wave was calculated by dividing the distance between the two edge streaks by the number of waves included between them. If cloud trains with clearly different wavelengths were found in an image, the cloud trains were recorded as two different lee waves.

Results and discussions

Figure 4a shows the seasonal variation in the number of cloud trains detected as described in "Materials and methods" section. Figure 4b–d shows the seasonal variations in the vertical profiles of water ice mass mixing ratio, zonal wind, and atmospheric temperature of the EMARS for 1400LT, respectively, obtained by

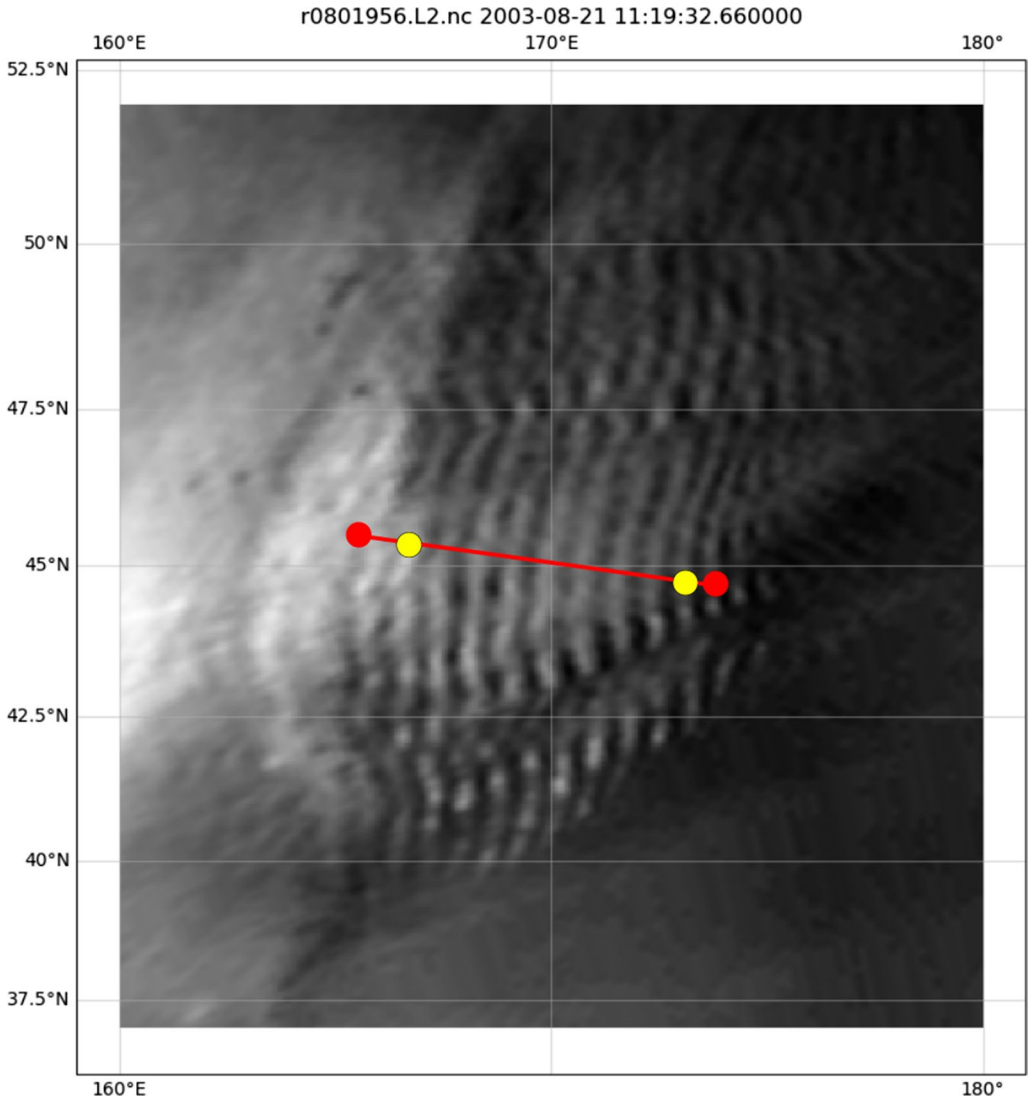

Fig. 3 The schematic view explaining the method for deriving the mean wavelength of the cloud train. The red circles indicate the two edge points of the cloud train that are determined so that the red line passing through them is as perpendicular as possible to the phase lines of the cloud streaks. The yellow circles indicate the most outside cloud streaks that can be visually detected on the red line

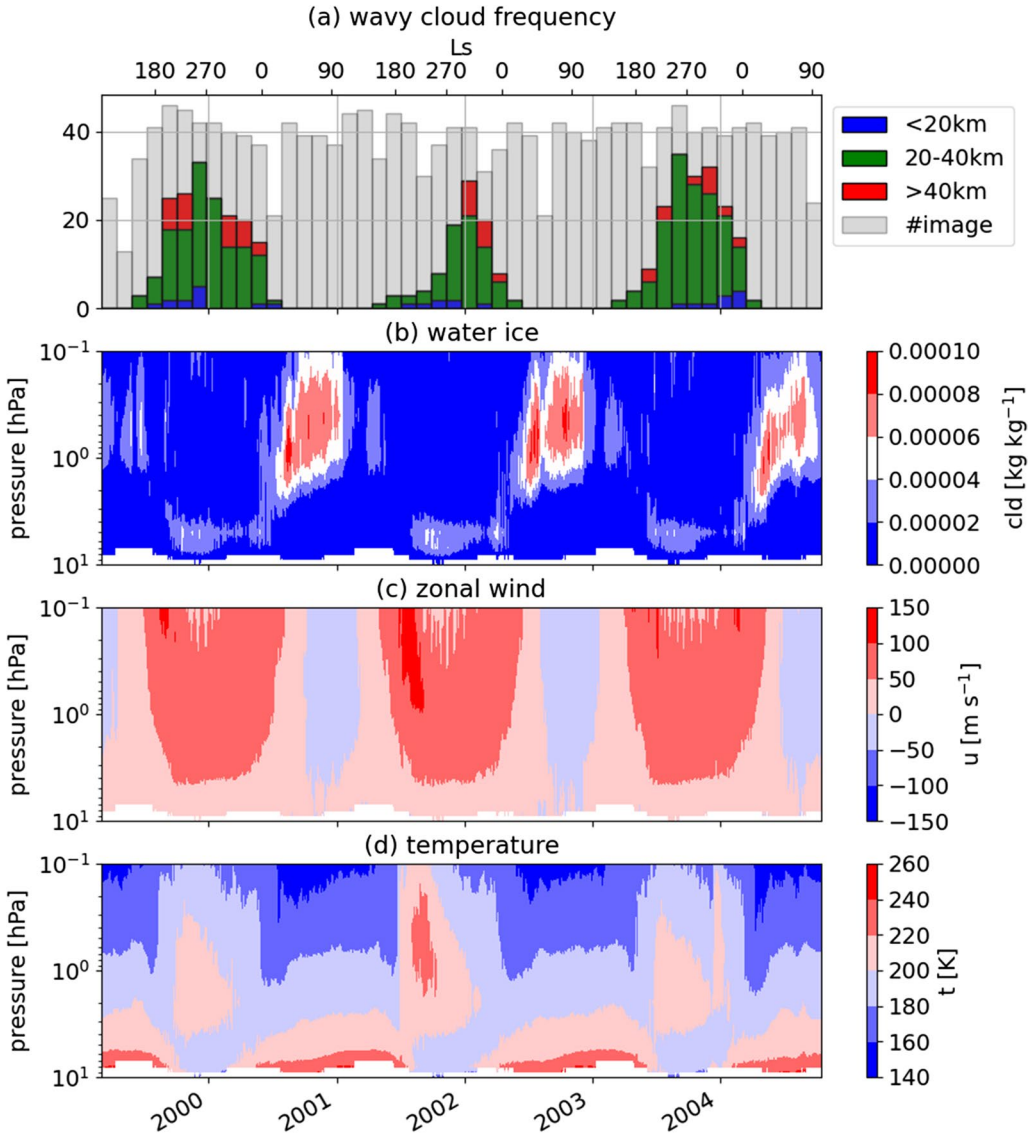

Fig. 4 The seasonal variabilities in the number of cloud trains and the background atmospheric variables. **a** The number of cloud trains, **b** water ice mixing ratio, **c** zonal wind, and **d** atmospheric temperature in the target area, WAP, are displayed. The gray bars in Panel **a** indicate the number of the MOC blue images available for this study. The blue, green, and red bars indicate the numbers of detected cloud trains whose wavelengths are short, middle, and long, respectively. The variables shown in Panels **b**, **c**, and **d** are derived from the EMARS 1.0 and interpolated into the pressure coordinate

horizontally averaging the variables in the region of 165°E–180°E and 30°N–50°N. Only the 14:00LT data were extracted from the database in order to be able to compare them with the frequency of the cloud trains, which were only observed at approximately 14:00LT by MGS. The variables defined on the sigma-p hybrid coordinate are interpolated into the pressure coordinate. Cloud trains are found in 531 out of 2476 MGS/MOC blue images (see Additional files 1 and 2) and clearly tend to be observed in the northern winter season. The typical wavelength of the associated lee waves is between 20 and 40 km and is consistent with the horizontal scale of the steep eastern slope of the mountain (Fig. 2). In the northern winter, the westerly jet is strong, and the atmospheric stability is high in the northern mid-latitudes. The atmospheric water vapor has to be close to saturation and upward wind has to be sufficiently large for clouds to form in this season. The northern winter low-level water ice clouds shown in Fig. 4b imply that the lower atmosphere in this region is sufficiently wet to allow cloud formation and the cloud can form even by modeled weak upward wind even

though the spatial resolution of the numerical model of the EMARS is too low to resolve the lee waves with horizontal wavelength of O (10 km). Therefore, it is quite possible for the cloud trains to be formed by the mountain lee waves on the eastern side of the Phlegra Montes.

Figure 4a also shows that few cloud trains were observed in the season from L_s (solar longitude) = 180° to L_s = 270° in Mars Year (MY) 25 due to the 2001 global dust storm (GDS). The result that the cloud trains were not detected during the 2001 GDS does not necessarily mean that the cloud trains did not occur during that period, but only that the increased optical thickness of the atmosphere made it impossible to determine whether cloud trains formed.

The theory of the vertical propagation of mountain waves was summarized by Durran (1986). The vertical structure of the perturbation vertical wind, $\widehat{w}$, is determined as follows:

$$\frac{\partial^2 \widehat{w}}{\partial z^2} + \left(l^2 - k^2\right)\widehat{w} = 0, \tag{1}$$

where $\widehat{w}$ and k are the vertically dependent amplitude of the vertical wind perturbation and the wavenumber in the direction parallel to a mean wind, respectively. Moreover, l^2 is the Scorer number for a stationary mountain wave and is defined as follows:

$$l^2 = \frac{N^2}{U^2} - \frac{1}{U}\frac{d^2U}{dz^2}, \tag{2}$$

where N and U are the Brunt-Väisälä frequency and the mean wind, respectively. l has the same dimension as wavenumber. Only gravity waves with wavenumbers smaller than l (wavelengths longer than $2\pi/l$) can propagate upward. This means that gravity waves with large wavenumbers (short wavelengths) can propagate upward only in the region where the stability is high (N is large) and the background mean wind is weak. Figure 5a and b shows the seasonal variations in the vertical profiles of N^2 and l^2, respectively, for 1400LT in the same region as shown in Fig. 4. The vertical coordinate of Fig. 5 does not indicate the same pressure level as in Fig. 4, but rather the approximate pressure of the sigma-p levels defined in the EMARS in order to avoid the degradation of the vertical resolution near the surface due to interpolation into the pressure coordinate. Here, N^2 is large below approximately 2 hPa (approximately 10 km) due to the high atmospheric stability in the northern winter, and the large N^2 extends far enough down to the lower levels for mountain waves to be excited by the Phlegra Montes. However, the Scorer number of a stationary mountain wave is extremely small, especially above 2 hPa, due to the strong westerly jet shown in Fig. 4c. Stationary waves with horizontal wavenumbers larger than l cannot propagate upward because the coefficient of the second term of Eq. (1) becomes negative. Therefore, the stationary waves with horizontal wavelengths shorter than $2\pi/l$ shown in Fig. 5c cannot propagate upward. For example, Fig. 5c shows that stationary waves having a horizontal wavelength that is shorter than 40 km are confined below 2 hPa, where it is sufficiently wet for clouds to form (Fig. 4b), in the northern winter. A long cloud train occurs when such a short wave is trapped in the lower atmosphere on the lee side of the mountain (Durran 1986). These can explain well the observational fact that the majority of the wavy cloud trains have wavelengths between 20 and 40 km, as shown in Fig. 4a. Observed cloud trains with shorter wavelengths are trapped closer to the surface, and cloud trains with longer wavelengths may reach up to approximately 10 km in the northern winter. Although lee waves with wavelengths much longer than 40 km may be excited, these waves do not contribute to the formation of long cloud trains with long wavelengths because these waves can propagate upward beyond the large l^2 altitudes. Parish et al. (2009) simulated the propagation of gravity waves using a linearized one-dimensional model and suggested the possibility of upward propagation of gravity waves and deposition of the momentum in the thermosphere. Their results predicted wave reflections between the evanescent region and the ground, whereas their simulations should not be compared straightforwardly with the present results because their results were limited to the northern polar region and the equator.

Heavens et al. (2020) revealed the global distributions of gravity wave activity in the Martian lower atmosphere using updated brightness temperature data observed by Mars Climate Sounder onboard the Mars Reconnaissance orbiter (MRO/MCS) in the A3 channel (635–665 cm^{-1}). Their off-nadir diagnoses for MY29-33 showed significant signals of gravity waves with wavelengths ranging from 10 to 100 km near the Phlegra Montes, whereas the observations they used were not sensitive to the lowest atmosphere below 10 km altitude. Their results support the results of the present study because the MCS might have detected lee waves with longer wavelengths propagating above 10 km. Heavens et al. (2022) used the A1 channel (595–615 cm^{-1}) of MRO/MCS and revealed the global distributions of gravity wave activity below 10 km. Their result showed the low gravity wave activity on the eastern side of the Phlegra Montes where cloud trains have been observed. The horizontal wavelengths claimed to be resolved in Heavens et al. (2020, 2022) seem to mean the wavelengths of gravity waves in the along-track direction. Both MGS and MRO are orbiting a frozen polar orbit. The phase lines (cloud streaks) of mountain

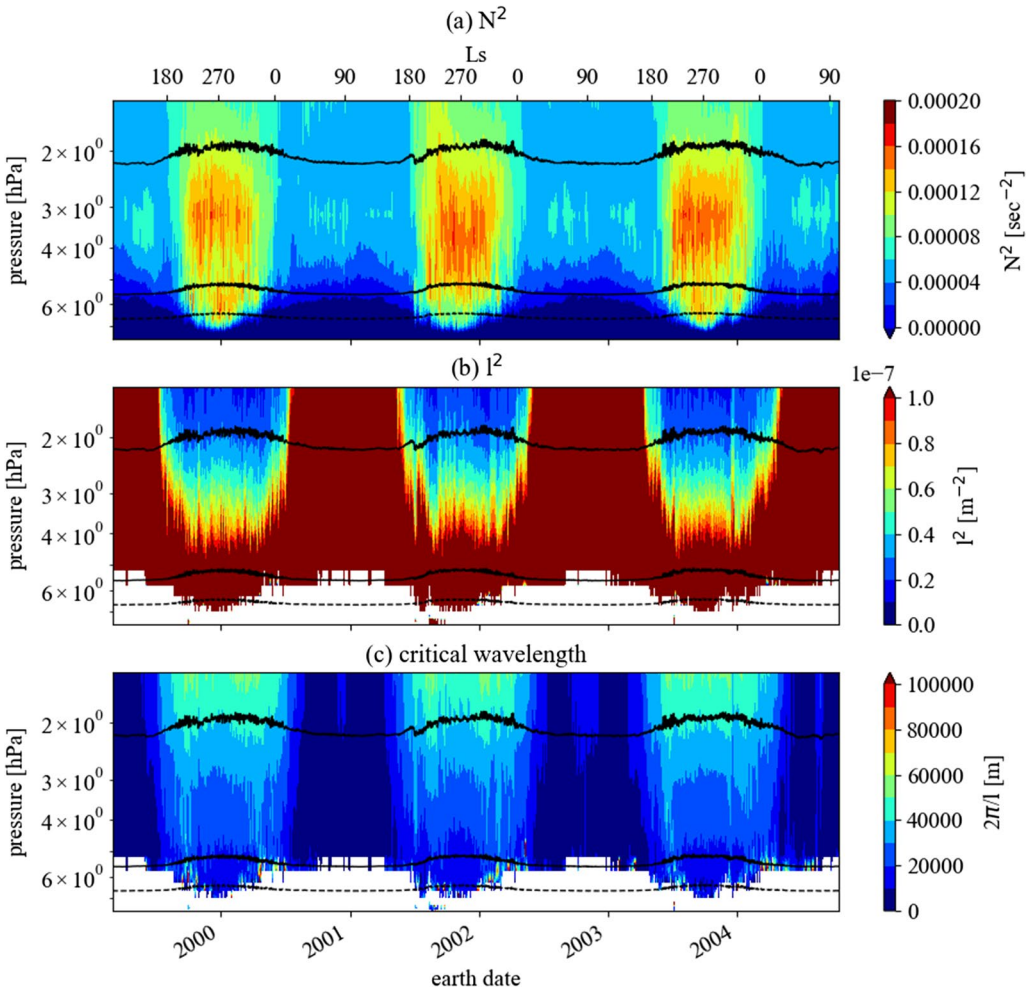

Fig. 5 The seasonal variations of the vertical profiles of the variables included in Eq. (2). **a** N^2, **b** l^2, and **c** $2\pi/l$ for 1400LT in the same region as Fig. 4 are displayed. The two solid and one dashed lines in each panel indicate the seasonal variations in geopotential height of 10 km, 0 km, and -2 km, respectively. The white areas in Panels **b** and **c** show the absolutely unstable layer near the surface

lee waves reported in the present study are approximately parallel to the latitudinal direction. Therefore, the wavelengths of the mountain lee waves in the along-track direction are much longer than 10–40 km. Because Fig. 6 of Heavens et al. (2022) shows the low visibility of such GWs below 10 km, the low gravity wave activity on the eastern side of the Phlegra Montes does not conflict with our results. Creasey et al. (2006) reported the regionality and seasonality of gravity wave activity estimated using occultation measurements from the MGS Radio Science (RS) experiment. The occultation results, which were sensitive to heights of 10–30 km, showed low gravity wave potential energy near the Phlegra Montes. However, no data for the northern mid-latitudes were available in the northern winter season, and the horizontal scale to which the observations are sensitive appears to be 100–1000 km (Heavens et al. 2020). Therefore, the results of the present study do not necessarily conflict with the results of the previous studies and reveal gravity wave activity associated with topography in the lowest atmosphere that has not yet been observed by any instruments.

Conclusion

The present study has revealed the climatology of cloud trains associated with the mountain lee waves on the eastern side of the Phlegra Montes, and we estimated the upper limit of altitudes where the lee waves propagate and the clouds form. The cloud trains were observed exclusively in the northern winter season, when the strong westerly jet develops and the atmosphere is stabilized and wet enough for clouds to form. Typical horizontal wavelengths of the cloud trains were 20–40 km and correspond to the steep eastern slope of the mountain. These wavelengths are also consistent

with the wavelengths of lee waves that are predicted to be trapped in the lower atmosphere from the vertical profile of the Scorer number, l^2. Figure 5c shows that a stationary wave with the horizontal wavelength of approximately 40 km cannot propagate to altitudes upper than about 10 km and that stationary waves with shorter wavelength are confined closer to the surface. Therefore, the observed cloud trains show that stationary lee waves are excited by the Phlegra Montes in the highly stable atmosphere and trapped below approximately 10 km due to the zonal wind vertical structure that increases rapidly with height. This requires numerical simulations that sufficiently resolve the steep topography and associated atmospheric phenomena with the horizontal scale of approximately 20 km to validate the results of the present study. Furthermore, the numerical models have to enable long lee waves to propagate upward and dissipate at the model top, keeping the mean wind profile realistic. Such difficult numerical simulations are left for future studies.

Abbreviations

ACB	Aphelion Cloud Belt
EMARS	The Ensemble Mars Atmosphere Reanalysis System
ISIS	Integrated Software for Imagers and Spectrometers
Ls	Solar longitude
MCS	Mars Climate Sounder
MGS	Mars Global Surveyor
MOC	Mars Orbiter Camera
MRO	Mars Reconnaissance Orbiter
MY	Mars Year
PDS	Planetary Data System
RS	Radio Science
WA	Wide angle
WAP	The western Arcadia Planitia

Supplementary Information

The online version contains supplementary material available at https://doi.org/10.1186/s40623-023-01767-x.

Additional file 1. List of MGS/MOC blue band images available for this study. This consists of five columns, image ID, observation time, orbit number, solar longitude, and filter name.

Additional file 2. List of cloud trains detected from images listed in Additional file 1. This consists of eight columns, observation date, image ID, orbit number, solar longitude, wavenumber, wavelength, longitude, and latitude.

Acknowledgements
The present study was supported by JSPS KAKENHI Grant Numbers JP20K04044 and JP20H01958.

Author contributions
KO prepared Mars image data, measured the wavelengths of cloud trains, investigated altitudes of the mountain waves and the cloud trains, and designed and completed the manuscript. MR visually extracted cloud trains from the Mars images prepared by KO and completed the list of the cloud trains. All the authors read and approved the final manuscript.

Funding
The present study was supported by JSPS KAKENHI to KO (Grant Numbers JP20K04044 and JP20H01958).

Availability of data and materials
The raw data used in the present study are available from the NASA Planetary Data System Imaging Node at https://pds-imaging.jpl.nasa.gov/data/mgs-m-moc-na_wa-2-sdp-l0-v1.0/. The image files used in the present study can be uniquely determined by image IDs listed in Additional file 1. The topography data shown in Fig. 2 were included in the Mars Climate Database 5.0 released from http://www-mars.lmd.jussieu.fr/mars/access.html (Millour et al. 2018). Version 4.2.0 of Integrated Software for Imagers and Spectrometers (ISIS) used for processing MGS/MOC images is preserved at Doi:10.5281/Zenodo.3962369 (Sucharski et al. 2020). The Ensemble Mars Atmosphere Reanalysis System (EMARS) version 1.0 is available at doi:10.18113/D3W375 (Greybush et al. 2018).

Declarations

Ethics approval and consent to participate
Not applicable.

Consent for publication
Not applicable.

Competing interests
The authors declare that they have no competing interest.

Author details
[1]Faculty of Science, Kyoto Sangyo University, Motoyama, Kamigamo, Kita-Ku, Kyoto, Japan.

Received: 25 October 2022 Accepted: 5 January 2023
Published online: 20 January 2023

References

Wang H, Ingersoll AP (2016) MGS MOC Mars Daily Global Maps, https://doi.org/10.7910/DVN/WWRT1V, Harvard Dataverse, V1
Conrath BJ, Pearl JC, Smith MD et al (2000) Mars Global Surveyor Thermal Emission Spectrometer (TES) observations: atmospheric temperatures during aerobreaking and science phasing. J Geophys Res 105:9509–9519
Cooper BA, Moores JE, Ellison DJ et al (2019) Constraints on Mars Aphelion Cloud Belt phase function and ice crystal geometries. Planet Space Sci 168:62–72. https://doi.org/10.1016/J.PSS.2019.01.005
Cooper BA, Moores JE, Battalio JM et al (2020) Aphelion Cloud Belt phase function investigations with mars color imager (MARCI). Planet Space Sci 184:104840. https://doi.org/10.1016/J.PSS.2020.104840
Creasey JE, Forbes JM, Hinson DP (2006) Global and seasonal distribution of gravity wave activity in Mars ' lower atmosphere derived from MGS radio occultation data. Geophys Res Lett. https://doi.org/10.1029/2005GL024037
Durran DR (1986) Mountainwaves. In: Ray PS (ed) Mesoscale meteorology and forecasting. American Meteorological Society, pp 472–492
Forget F, Hourdin F, Fournier R et al (1999) Improved general circulation models of the Martian atmosphere from the surface to above 80 km. J Geophys Res 104:24155–24175
Greybush SJ, Kalnay E, Wilson RJ et al (2019) The ensemble mars atmosphere reanalysis system (EMARS) version 1.0. Geosci Data J 6:137–150. https://doi.org/10.1002/gdj3.77
Greybush SJ, Kalnay E, Wilson RJ, et al (2018) The ensemble mars atmosphere reanalysis system (EMARS) version 1.0 dataset. https://www.datacommons.psu.edu/commonswizard/MetadataDisplay.aspx?Dataset=6171. https://doi.org/10.18113/D3W375
Guha BK, Panda J, Wu Z (2021) Observation of aphelion cloud belt over Martian tropics, its evolution, and associated dust distribution from MCS data. Adv Sp Res 67:1392–1411. https://doi.org/10.1016/J.ASR.2020.11.010

Guzewich SD, Toigo AD, Kulowski L, Wang H (2015) Mars Orbiter Camera climatology of textured dust storms. Icarus 258:1–13. https://doi.org/10.1016/j.icarus.2015.06.023
Guzewich SD, Toigo AD, Wang H (2017) An investigation of dust storms observed with the Mars Color Imager. Icarus 289:199–213. https://doi.org/10.1016/j.icarus.2017.02.020
Heavens NG, Kass DM, Kleinböhl A, Schofield JT (2020) A multiannual record of gravity wave activity in Mars's lower atmosphere from on-planet observations by the Mars Climate Sounder. Icarus 341:113630. https://doi.org/10.1016/j.icarus.2020.113630
Heavens NG, Pankine A, Battalio JM et al (2022) Mars climate sounder observations of gravity-wave activity throughout Mars's lower atmosphere. Planet Sci J 3:57. https://doi.org/10.3847/psj/ac51ce
Kulowski L, Wang H, Toigo AD (2017) The seasonal and spatial distribution of textured dust storms observed by Mars Global Surveyor Mars Orbiter Camera. Adv Sp Res 59:715–721. https://doi.org/10.1016/j.asr.2016.10.028
Malin MC, Edgett KS, Cantor BA et al (2010) An overview of the 1985–2006 Mars Orbiter Camera science investigation. Mars 5:1–60. https://doi.org/10.1555/mars.2010.0001
Michaels TI, Colaprete A, Rafkin SCR (2006) Significant vertical water transport by mountain-induced circulations on Mars. Geophys Res Lett 33:1–5. https://doi.org/10.1029/2006GL026562
Millour E, Forget F, Spiga A, et al (2018) The Mars Climate Database (version 5.3). In: Scientific workshop: "From Mars Express to ExoMars." Madrid, pp 27–28
Montmessin F, Forget F, Rannou P et al (2004) Origin and role of water ice clouds in the Martian water cycle as inferred from a general circulation model. J Geophys Res 109:1–26. https://doi.org/10.1029/2004JE002284
Ogohara K, Satomura T (2011) Numerical simulations of the regional characteristics of dust transport on Mars. Adv Sp Res 48:1279–1294. https://doi.org/10.1016/j.asr.2011.06.008
Ogohara K, Munetomo T, Hatanaka Y, Okumura S (2016) Automated detection of Martian water ice clouds using Support Vector Machine and simple feature vectors. Planet Space Sci 134:64–70. https://doi.org/10.1016/j.pss.2016.10.009
Parish HF, Schubert G, Hickey MP, Walterscheid RL (2009) Propagation of tropospheric gravity waves into the upper atmosphere of Mars. Icarus 203:28–37. https://doi.org/10.1016/j.icarus.2009.04.031
Sucharski T, Mapel J, Jcwbacker, et al (2020) USGS-Astrogeology/ISIS3: ISIS 4.2.0 Public Release (4.2.0)
Wang H, Ingersoll AP (2002) Martian clouds observed by Mars Global Surveyor Mars Orbiter Camera. J Geophys Res 107:1–16. https://doi.org/10.1029/2001JE001815
Wilson RJ, Neumann GA, Smith MD (2007) Diurnal variation and radiative influence of Martian water ice clouds. Geophys Res Lett 34:1–4. https://doi.org/10.1029/2006GL027976

Publisher's Note